

pubs.acs.org/Biomac Article

# Competition between $\beta$ -Sheet and Coacervate Domains Yields **Diverse Morphologies in Mixtures of Oppositely Charged Homochiral Polypeptides**

Nairiti J. Sinha, Keila Cristina Cunha, Robert Murphy, Craig J. Hawker, Joan-Emma Shea, and Matthew E. Helgeson\*



Cite This: https://doi.org/10.1021/acs.biomac.3c00361



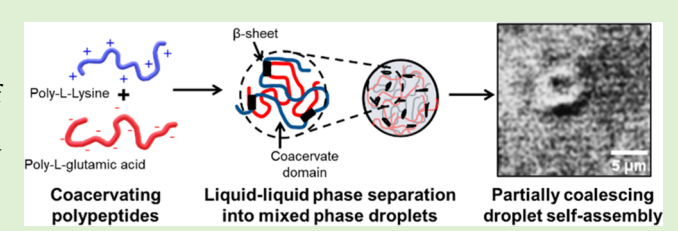
**ACCESS** I

III Metrics & More

Article Recommendations

Supporting Information

ABSTRACT: Biomolecular assembly processes involving competition between specific intermolecular interactions and thermodynamic phase instability have been implicated in a number of pathological states and technological applications of biomaterials. As a model for such processes, aqueous mixtures of oppositely charged homochiral polypeptides such as poly-L-lysine and poly-Lglutamic acid have been reported to form either  $\beta$ -sheet-rich solidlike precipitates or liquid-like coacervate droplets depending on



competing hydrogen bonding interactions. Herein, we report studies of polypeptide mixtures that reveal unexpectedly diverse morphologies ranging from partially coalescing and aggregated droplets to bulk precipitates, as well as a previously unreported reentrant liquid-liquid phase separation at high polypeptide concentration and ionic strength. Combining our experimental results with all-atom molecular dynamics simulations of folded polypeptide complexes reveals a concentration dependence of  $\beta$ -sheet-rich secondary structure, whose relative composition correlates with the observed macroscale morphologies of the mixtures. These results elucidate a crucial balance of interactions that are important for controlling morphology during coacervation in these and potentially similar biologically relevant systems.

#### ■ INTRODUCTION

Highly charged peptides and proteins have been extensively investigated for their self and complex coacervation behavior in diverse biological contexts. For example, peptide domains in intrinsically disordered proteins (IDP) participate in intracellular liquid-liquid phase separation to form membraneless compartments that provide unique environments for various cellular functions. <sup>1-3</sup> Misfolding of IDPs into  $\beta$ -sheet-rich amyloid fibrils has been linked to pathological pathways in many neurodegenerative diseases. 1,4 More recently, interest in polypeptide coacervation has followed from demonstrations of protocells of coacervating peptides, which have been implicated in proposed origin-of-life scenarios. 5-7 Finding optimal conditions for peptide coacervation in primordial environments is crucial for corroborating this theory. From a technological standpoint, polypeptide coacervate materials are being investigated for the discovery of superior biocompatible underwater adhesives and drug-delivery carriers.<sup>8-10</sup> Consequently, non-natural and naturally occurring peptides displaying varying degrees of complexity in geometry, chirality, and sequence, as well as external factors such as electrolyte type and concentration, temperature, and presence of macromolecular crowding agents have been investigated to understand the coacervation behavior using a combination of theory, simulations, and experiments.<sup>7,10-22</sup>

Peptides differ from synthetic polyelectrolytes due to their inherent propensity to form unique, hydrogen-bonded secondary, tertiary, and quaternary structures. As a result, the affinity of the peptide backbone to form specific hydrogen bonds has to be explicitly incorporated in the theory of peptide and protein folding. 23-25 However, competition between hydrogen bonding and electrostatic interactions during peptide coacervation is yet to be formalized. An emerging consensus in recent studies on peptide coacervation is that competition between  $\beta$ -sheet aggregation and liquid—liquid phase separation results in either solid-like assemblies or liquid-like droplets.<sup>6,16</sup> Specifically, in experiments involving complex coacervation in aqueous mixtures of long-chain homopolymeric peptides, i.e., polypeptides of poly-L-lysine and poly-Lglutamic acid in the presence of added sodium chloride salt, Tirrell and co-workers used optical microscopy and secondary structure measurements to investigate the preference for solidlike precipitates over liquid-like coacervate droplets. 11,16,17,26

Received: April 9, 2023 Revised: June 21, 2023



The formation of precipitates was mitigated by utilizing synthetic analogs containing alternating D<sub>1</sub>L-amino acids in the backbone; 16 the recovery of liquid-like droplet morphologies indicated that hydrogen-bonding-driven  $\hat{\beta}$ -sheet formation results in hydrophobic self-assembly and precipitation. 14, By contrast, Prifitis et al. were able to isolate liquid-like droplets in aqueous homochiral polypeptide mixtures by controlling the polypeptide mixing process. 11,12 Importantly, Pacalin et al. showed that the sequence of chirality along the polypeptide backbone impacts the droplet-to-precipitate behavior in polypeptide coacervate mixtures.<sup>27</sup> In yet another study, Keating and co-workers investigated mixtures of poly-Llysine and poly-L-glutamic acid of varying lengths and showed that under specific solution conditions, the polypeptide length impacted the morphology wherein shorter polypeptide pairs formed single-phase mixtures or coacervate droplets whereas longer polypeptide pairs formed precipitates.

To explain the experimental observations, molecular dynamics (MD) simulations have been employed to investigate the nanostructure of coacervating polypeptide complexes. Perry et al. performed MD simulations of a 10-mer polypeptide complex in water and showed that the complex spontaneously folded into an antiparallel  $\beta$ -sheet. However, more recent MD simulations investigating homochiral polypeptide complexation have reported contradictory results with respect to  $\beta$ -sheet formation that are sensitive to the type of force field, polypeptide length, and counterion type. A deeper understanding of the coacervation of homochiral polypeptide mixtures will not only address such contradictions between experimental and simulation results but also add to our understanding of the theory of coacervation.

In an attempt to resolve some of these complexities, this work involves a systematic investigation of coacervation in stoichiometric (1:1) charge ratio mixtures of oppositely charged 100-mer polypeptides of poly-L-lysine (polycation) and poly-L-glutamic acid (polyanion) under dilute and semidilute aqueous solution conditions and in the presence of added sodium chloride salt. We show that a concentrationdependent interplay of intra- and intermolecular peptidepeptide interactions dictates the coacervate morphologies that range from partially coalescing droplets to colloidal aggregates of droplets to bulk precipitates that are readily viewable using optical microscopy. All-atom molecular dynamics simulations are used to link the nanostructure of the polypeptide complex to the macroscale morphology of the polypeptide mixtures. Importantly, the results suggest that both  $\beta$ -sheet and coacervate domains coexist in the folded polypeptide complex, in a manner that is sensitive to the concentration of polypeptide/salt and that dictates the observed morphologies upon mixing. These new results shed light on the balance of secondary structures controlling morphology in coacervating polypeptide mixtures.

# **■** METHODS

Experiments. Polypeptide Synthesis and Purification. BLG and ZLL NCAs were prepared using literature procedures<sup>28</sup> and were of high purity as confirmed by <sup>1</sup>H NMR spectroscopy (Figures S1 and S2). Using Li-HMDS-initiated N-carboxyanhydride (NCA) ring opening (ROP), both PBLG and PZLL with a target degree of polymerization (DP) of 100 were prepared.<sup>29</sup> End capping using 2,2-dimethylpropionic anhydride allowed for quantitative characterization of DPs via end-group analysis of <sup>1</sup>H NMR spectra with PBLG (Figure S3) and PZLL (Figure S4) having DPs of 120 and 110, respectively.

Polypeptides were prepared with good control of molecular weight and narrow dispersity, observable in single diffusion coefficients as noted in DOSY NMR spectroscopy (Figure S5) and monomodal gel permeation chromatography (GPC) (Figure S6). Deprotection afforded the ionizable polypeptides (Figures S7 and 1A) in good

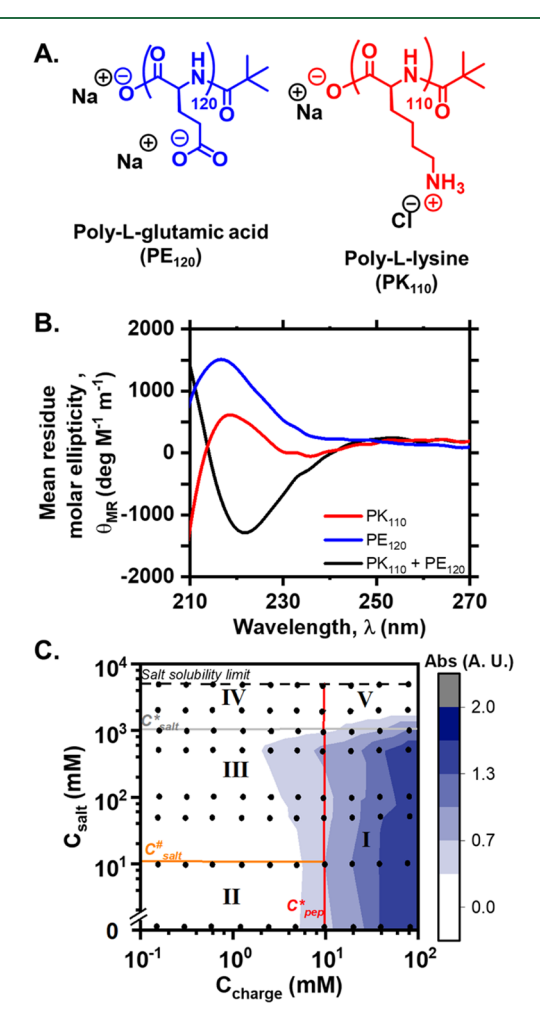


Figure 1. (A). Chemical structure of poly-L-lysine (PK) and poly-Lglutamic acid (PE). Subscripts are <sup>1</sup>H NMR estimates of the degree of polymerization. Polypeptides were neutralized and dialyzed, which resulted in their polypeptide salts. (B) Circular dichroism spectroscopy of polypeptides dissolved in water. Spectrum for 0.06 wt % total polypeptide concentration (4 mM charged residue concentration) is shown here. Individual polypeptide solutions are random coils, and 1:1 mixture adopts a  $\beta$ -strand secondary structure. (C) Map of the absorbance (Abs) of mixtures at a wavelength of 500 nm in a space of total 1:1 charged residue ( $C_{\rm charge}$ ) and added salt ( $C_{\rm salt}$ ) concentrations. Here,  $C_{\rm pep}^*$ ,  $C_{\rm salt}^*$ , and  $C_{\rm salt}^*$  are the critical polypeptide concentration, threshold salt concentration, and critical salt concentration respectively (1 mM =  $10^{-3}$  M). The black dots indicate compositions at which spectroscopy and microscopy measurements were performed in a 96-well plate. The five regions shown are the following: (I) bulk precipitation, (II) LLPS into partially coalescing droplets, (III) colloidal aggregation of coacervate droplets, (IV) single phase, and (V) re-entrant LLPS.

yield, and extensive dialysis against distilled water (four times over 2 days) ensured control over purity and counterion type (sodium and chloride ions). Molecular characterization results for individual polypeptides (nuclear magnetic resonance spectroscopy before and after deprotection and gel permeation chromatograms) are given in the Supporting Information (SI).

Sample Preparation. Stock solutions of poly-L-lysine and poly-Lglutamic acid were prepared at the desired polypeptide and concentration of sodium chloride in Milli-Q water. Polypeptide mixtures were prepared by directly mixing individual polypeptide stock solutions in a 96-well plate by initially adding 25  $\mu$ L of polylysine, followed by 25  $\mu$ L of polyglutamic acid and pipette mixing for 15 s. The prepared 96-well plates were used for ultraviolet-visible (UV-vis) spectroscopy and optical microscopy measurements after equilibrating the mixtures for 24 h. It should be noted that absorbance at 500 nm is measured as an indicator of turbidity and is a qualitative measurement that cannot be used as a true measure of phase boundaries. Thus, low turbidity of the solution indicates sparse or no morphologies formed after mixing, and high turbidity indicates bulk phase separation. Optical microscopy images were acquired over 5 days after mixing. Minimal to no changes were observed in optical micrographs of the mixtures after 24 h of mixing and for the remaining duration of experiments. Experiments were repeated three times to ensure the reproducibility of results.

Characterization of Polypeptide Morphologies. The absorbance of polypeptide mixtures in the 96-well plate was measured on a Tecan Spark 10 M Multimode Plate Reader at 500 nm. The secondary structure of the polypeptides was characterized using circular dichroism spectroscopy (Jasco J-1500 CD Spectrapolarimeter) using a 1 mm path length quartz cuvette. Phase-contrast optical micrographs were acquired on a Zeiss Axio Observer optical microscope in transmission mode using 20x, 40x, and 60x air lenses. Two to four points were randomly picked by the microscope software in each well and time-lapse videos at a 30 Hz acquisition rate as well as Z-stack micrographs were captured using a Zeiss Axiocam camera. ImageJ2's FIJI image analysis software was used for processing micrographs. 30 The videographs were acquired at multiple heights from the bottom of the well; it is inherently difficult to focus on all droplets at a given height due to the combined turbidity and thickness of the samples. Select time-lapse videos of polypeptide solutions in different wells are included in SI Videos vS1, vS2, vS3, vS4, vS5, vS6, and vS7.

Simulations. Systems and Box Size. Our systems were composed of a 100-mer lysine and a 100-mer glutamic acid, both capped with a t-butyl N-termina and explicitly solvated with SPC water molecules.<sup>31</sup> The parameters used for the Na<sup>+</sup> and Cl<sup>-</sup> ions were developed by Loche et al.<sup>32</sup> The polypeptides were built as completely extended chains and 5 ns simulations of each one were performed to obtain more compact structures. In these simulations, each polypeptide was individually placed diagonally in a 25 nm cubic box, and Na<sup>+</sup> or Cl<sup>-</sup> ions were added to counterbalance the charges. The final structure of each polypeptide was then placed perpendicular to each other and about 9 nm distant in a 35 nm cubic box, which corresponds to the 0.1 wt % polypeptide concentration. Next, the system had the energy minimized, and the temperature and pressure equilibrated, as described in the Molecular Dynamics Simulations section below. The structure obtained after the equilibration of the 0.1 wt % system was more compact and it could be placed slightly diagonally in a 16.2 nm cubic box, which corresponds to the 1.0 wt % polypeptide concentration. A total of 102 Na+ ions and 100 Cl- ions were added

Molecular Dynamics Simulations (MD). Simulations were performed using the new GROMACS 2019.6 simulation suite under an NPT ensemble and the GROMOS 53A6 force field.3 After each system was built, energy minimization was carried out using the steepest descent algorithm for 100,000 steps or until it reached the convergence energy criterion of 750 kJ/mol/nm. Next, the simulations were slowly heated, increasing the temperature linearly, from 0 to 300 K for 10 ns using the velocity-rescaling thermostat and a 1 ps time constant. The positions of heavy atoms in the polypeptide were initially restrained using a force of 1000 kJ/mol/ nm<sup>2</sup> in all directions. An NVT ensemble was used during this step. Afterward, the pressure was equilibrated through an unrestrained NPT simulation during 10 ns. In this step, we used the same temperature coupling condition as in the temperature equilibration and a Berendsen barostat to couple pressure isotropically at 1 bar and 1 ps time constant. In the equilibration runs, we also used a cutoff of 1.0 nm for both electrostatic and van der Waals (vdW) interactions. The other conditions used in the above-mentioned steps are the same as will be described for the production runs. The final simulations were performed from 0.5 to 1  $\mu$ s, depending on the system. The temperature of 300 K was controlled using the Nose-Hoover thermostat with a 1.0 ps coupling constant. The pressure was coupled isotropically using the Parrinello-Rahman barostat with a 2.0 ps time constant. The isothermal compressibility of  $4.5 \times 10^{-5} \text{ bar}^{-1}$  was used. Water bonds were kept rigid using the SETTLE algorithm.<sup>34</sup> A real-space cutoff of 1.2 nm was used for both electrostatic and van der Waals (vdW) interactions, which is also the range of our neighbor list. This neighbor list was updated each 5th timestep, using a grid description for the distribution of particles. Long-range electrostatics are computed according to the Particle Mesh Ewald (PME) algorithm. 35,36 A shift-function formalism will be used for calculating the vdW interactions. The leapfrog algorithm with a timestep of 2 fs is used to integrate the equations of motion. A Verlet cutoff scheme was used for neighbor searching, with nonbonded pairs updated every 10 steps.37

Data Analysis. The analysis of the molecular dynamic trajectories was performed using the standard tools available with the package GROMACS. Relevant conformations were identified through the Daura algorithm for clustering structures. A cluster was obtained within an empirically defined root-mean-square deviation (RMSD) cutoff (2 Å) based on nonterminal backbone atoms within the Daura algorithm. The secondary structure was obtained through the DSSP algorithm (gmx do\_dssp). Gmx gyrate was used to obtain the radius of gyration ( $R_{\rm g}$ ).

#### RESULTS

Oppositely charged polypeptides poly-L-lysine (PK) and poly-L-glutamic acid (PE) of target degree of polymerization 100 were synthesized using N-carboxyanhydride ring-opening polymerization (NCA ROP) of their respective side-chainprotected NCA monomers (see the Methods Section). The use of NCA ROP method is advantageous relative to conventional solid-phase synthesis due to its ability to synthesize gram scales of polypeptides that have more than 40 amino acid repeat units, albeit with decreased control over dispersity and sequence.41 The chemical structures of the sodium and chloride salts of PE and PK, respectively, are shown in Figure 1A (see the Supporting Information (SI) for molecular characterization of synthesized polypeptides). Lyophilized polypeptides were mixed at a stoichiometric (1:1) charge ratio in Milli-Q water at a sodium chloride (NaCl) salt concentration, C<sub>salt</sub>, ranging from 0 M (no added salt) to 5 M (NaCl solubility limit). The polypeptide concentration,  $C_{\text{pep}}$ , varied from 0.001 to 1.0 wt % corresponding to a total charged residue concentration, C<sub>charge</sub>, in the range of 0.1-80 mM, respectively. The mixtures were evaluated for their secondary structure, absorbance at 500 nm, and morphology using circular dichroism, UV-vis spectroscopy, and optical microscopy, respectively.

Circular dichroism (CD) spectra (Figure 1B) indicate that whereas the individual polypeptides adopt a random coil conformation (indicated by the positive absorbance band in the 210–230 nm range), the charge-matched mixtures formed  $\beta$ -sheets indicated by a single negative absorbance band with a minimum near 220 nm. <sup>42</sup> Thus, the mixtures contain  $\beta$ -sheet-rich complexes of poly-L-lysine and poly-L-glutamic acid chains, consistent with previous studies. Interestingly,  $\beta$ -sheet secondary structure was recorded to varying degrees for all polypeptide mixtures (see Figure S8). Further analysis of CD spectra was not pursued due to the potential corruption of the spectra due to wavelength-dependent light scattering for the

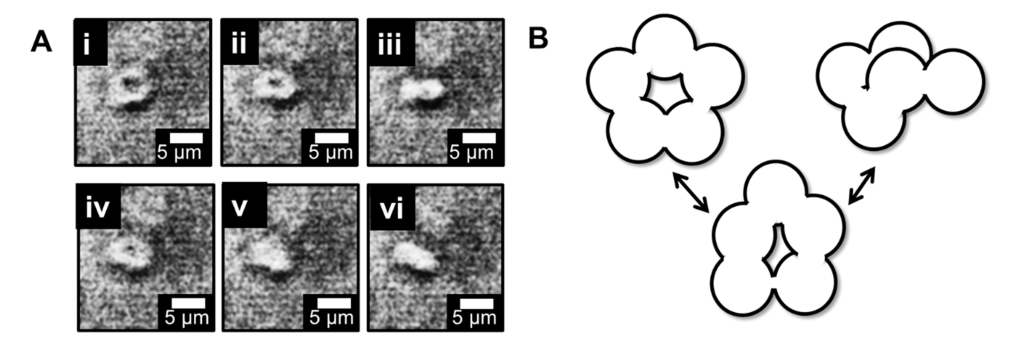


**Figure 2.** (A) Optical micrographs showing a dynamic assembly of partially coalesced coacervate droplets. The images were acquired in region II  $(C_{\text{pep}} \sim 0.01 \text{ wt }\%, C_{\text{salt}} = 0)$ . Representative snapshots are shown here (i-vi). (B) Schematic of partially coalescing droplets that form assemblies in (A). Individual droplets can be resolved in the assemblies that change shape over time.

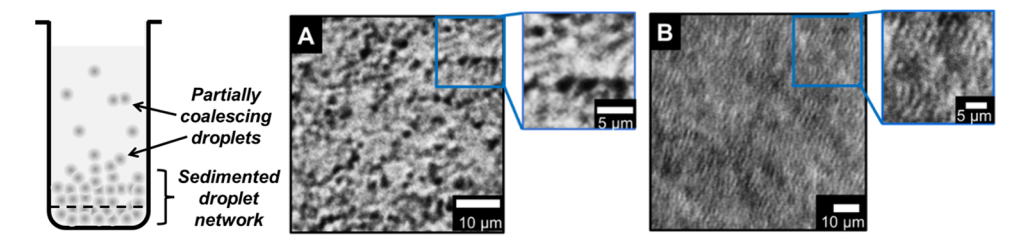


Figure 3. Optical microscopy of the sedimented network of partially coalescing droplets. The schematic on the left depicts a well with a sedimented network of partially coalescing droplets. Snapshots of the dense phase (shown as a dashed line in the schematic) at  $C^*_{pep} \sim 0.5$  wt % and (A) No  $C_{salt}$  and (B) 10 mM  $C_{salt}$ . Insets are zoomed images of the indicated region of the micrographs wherein individual droplets can be resolved within the network.

phase-separating turbid solutions that were investigated in this study. Optical absorbance at 500 nm for a range of  $C_{\rm salt}$  versus  $C_{\rm charge}$  indicates the turbidity of the polypeptide mixture (Figure 1C) and suggests that phase separation occurs above a critical polypeptide concentration  $C^*_{\rm pep} \approx 0.1$  wt % ( $C_{\rm charge} \approx 10$  mM) and below a critical salt concentration  $C^*_{\rm salt} \approx 1$  M.

Extensive optical microscopy within this composition space was used to precisely determine the corresponding state boundaries in the mixtures. Results indicated the existence of five regions with distinct morphologies (regions I–V in Figure 1C). Region I identified by absorbance measurements, i.e.,  $C_{\rm pep} > C^*_{\rm pep}$  and  $C_{\rm salt} < C^*_{\rm salt}$  consisted of bulk precipitates with a sheet-like morphology (see SI Video vS1). Such morphologies are consistent with precipitates that have been reported previously. <sup>14,16,17</sup>

The morphologies observed in the remainder of the composition space differ from those previously reported in the literature and are further classified into four regions with distinct morphologies. In region II, droplet-like morphologies are observed (see Videos vS2–vS5). In region III, colloidal aggregates of droplets are observed (see SI Video vS6), with a transition at a threshold salt concentration  $C_{\rm salt}^{\#} \sim 10$  mM NaCl. A single-phase solution (region IV in Figure 1C) exists above  $C_{\rm salt}^*$ . In high ionic strength and concentrated polypeptide solution ( $C_{\rm pep} > C_{\rm pep}^*$ ) region V in Figure 1C), liquid-like droplets are observed (for videos, see Video vS7). Further evidence of the morphological behavior of solutions in these regimes is provided below.

Low Ionic Strength Regime ( $C_{\rm salt}$  <  $C_{\rm salt}^{\#}$ , Region II). The poly-L-Lysine and poly-L-glutamic acid mixtures with no added salt displayed morphologies that were classified broadly into bulk precipitates in concentrated conditions (region I) and liquid-like droplets in dilute conditions (region II), with a transition near a critical polypeptide concentration,  $C^*_{\rm pep} \sim 0.1$ 

wt % ( $C_{\rm charge} \sim 10$  mM). Interestingly, unlike coacervating droplets that coalesce into droplets of varying sizes, dynamically fluctuating assemblies of partially coalescing droplets were observed in region II (Figure 2A).

Liquid droplets that have similar sizes can resist Ostwald ripening due to identical Laplace pressure gradients on their surface; however, resistance to full coalescence after contact neck formation between droplets is indicative of a higher viscosity in the droplet interior. Furthermore, the dynamic nature of the partially coalescing droplet assemblies (see Figure 2A,B) indicates that, regardless of the molecular structure and dynamics of polypeptides within the dense phase, the overall properties of the assemblies remain liquid-like. 9,44 Assembly shape changes over time may be dictated by the delicate interplay between solid-like and liquid-like phases that coexist within them

As  $C_{\rm pep}$  increases and approaches  $C^*_{\rm pep}$ , the turbidity of the solution increases, indicating an increase in the volume fraction of the droplets. Under these conditions, a dense layer with a dynamic bulk morphology is observed at the bottom of the container that is reminiscent of a fluctuating network of partially coalesced droplets (snapshots are shown in Figure 3A,B, and time-lapse videos are given in Videos vS3–vS5). It is important to note that the morphologies reported here form spontaneously after mixing and do not change significantly over a month after mixing based on optical microscopy and spectroscopy measurements. The aging behavior of these mixtures over longer periods of time will be undertaken in a future study. Furthermore, since the dynamic networks sediment to the bottom of the well, surface interactions may be responsible for differences in their morphologies (Figure 3).

Moderate lonic Strength Regime ( $\overline{C}^*_{salt} < C_{salt} < C_{salt}^*$ , Region III). The impact of added salt on the morphology of polypeptide mixtures is shown in Figure 4 for  $C_{pep} < C^*_{pep}$ 

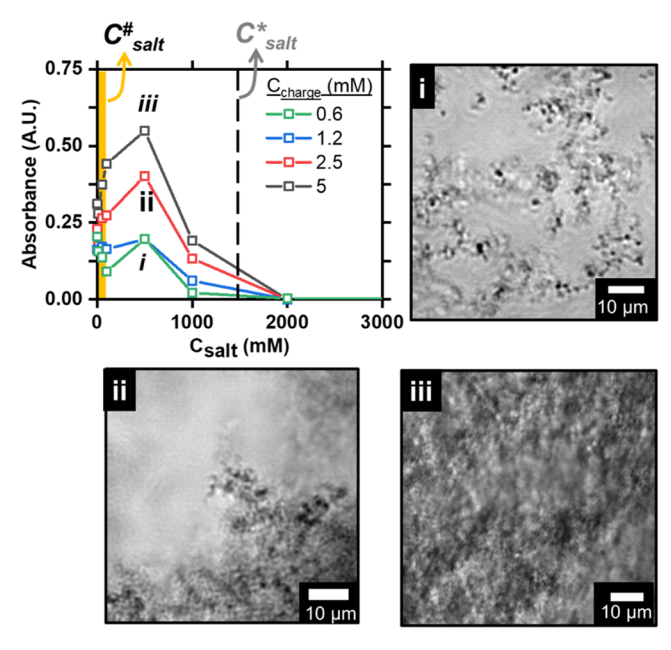


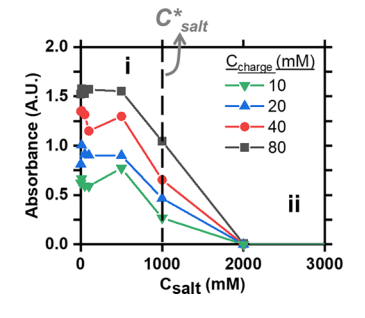
**Figure 4.** Morphologies observed in dilute polypeptide mixtures with added salt. The plot of absorbance at 500 nm as a function of salt at dilute polypeptide concentrations ( $C_{\rm pep} < C^*_{\rm pep}$ ) shows a decrease in the volume fraction of coacervating droplets with the addition of salt at  $C_{\rm salt} > C_{\rm salt}^{\#}$ . Optical micrographs indicate the presence of diffuse colloidal aggregate-like morphologies (i) for  $C_{\rm pep} \ll C^*_{\rm pep}$ , dense colloidal aggregates of droplets (ii), and volume-spanning aggregate networks (iii) as  $C_{\rm pep}$  approaches  $C^*_{\rm pep}$ .

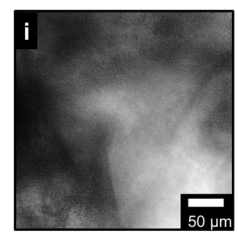
(region III). For a fixed polypeptide concentration in this regime, above a threshold concentration of added sodium chloride salt,  $C_{\rm salt}^{\ \ \ }\sim 10$  mM, an initial increase in turbidity with added salt of up to  $\sim \! 100$  mM is observed, indicating an increase in the optical density of scatterers. Optical microscopy indicates the formation of solid-like precipitates or colloidal aggregates of coacervates in this regime (Figure 4i), similar to previous reports. As the concentration of polypeptide is further increased at a fixed salt concentration, the turbidity also increases reflecting an increase in the volume fraction of the colloidal aggregates. Concomitantly, a transition from compact colloidal aggregates of solid-like droplets to a volume-spanning condensed network of aggregates is seen in the optical micrographs (Figure 4ii,iii). Finally, beyond  $C^*_{\rm pep}$ , the precipitate morphology of region I is found.

The decreasing turbidity of solutions with increasing salt concentration is consistent with expectations of coacervating macromolecules, i.e., as one approaches the upper critical point of the phase boundary between the dense and dilute phases, the amount of dense phase decreases. Thus, the overall volume fraction of colloidal aggregates is expected to decrease with increasing salt concentration. Above a critical salt concentration  $C^*_{\text{salt}}$ , we observe a transition from region III to region IV, wherein a single phase exists and no droplets or precipitates are observable via optical microscopy.

High Ionic Strength Regime  $(C_{salt} > C_{salt}^*, Regions IV)$ and V). Above the critical salt concentration  $C^*_{\text{salt}}$ , two regimes are observed. For dilute polypeptide solutions (  $C_{\rm pep}$  < $C^*_{pep}$ , region IV), a single homogeneous solution phase is recorded. For concentrated polypeptide solutions ( $C_{pep}$  >  $C^*_{pep}$ , region V), the turbidity of the polypeptide mixtures in region I (Figure 5i) decreases with added salt. Above  $C_{\text{salt}}^*$ , a transition into a state of liquid-liquid phase separation (LLPS) is observed, marked by a transition from bulk precipitates to droplets in optical microscopy (Figure 5ii). The volume fraction of droplets in this re-entrant LLPS is small and results in immeasurable turbidity of the solution. We, therefore, conclude that a large fraction of polypeptide complexes exists in the coexisting solution phase and a small fraction of complexes associate and form droplets in this composition range. This behavior of polypeptide mixtures has not been reported before to the best of our knowledge (see Video vS7 for time-lapse videos).

All-Atom Molecular Dynamics Simulations of Polypeptide Complexes. To investigate the molecular structure of the polypeptide complexes and their dependence on solution composition, we performed all-atom MD simulations in explicit water of a complex of poly-L-Lysine with 1:1 chloride ions (100 repeat units) and poly-L-glutamic acid with 1:1 sodium ions (100 repeat units). Simulations were performed at two polypeptide concentrations, 0.1 wt % (8 mM charged residues) and 1 wt % (80 mM charged residue) corresponding to regions II and I, respectively, to capture the impact of polypeptide concentration on the structure of the polypeptide complex. The simulations of the two polypeptide concentrations were obtained by simulating different box sizes under periodic boundary conditions and, consequently, the number of water molecules. The systems were initiated from extended structures of the polypeptides at a distance of ~9 nm from each other within the simulated volume. Simulations were performed for 0.5  $\mu$ s for  $C_{pep}$  = 0.1 wt % (8 mM charge





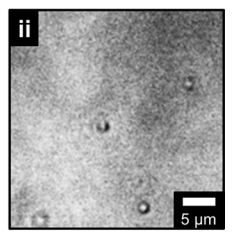


**Figure 5.** Morphologies observed in concentrated polypeptide mixtures with added salt. The plot of absorbance at 500 nm as a function of salt at concentrated polypeptide concentrations ( $C_{\text{pep}} > C^*_{\text{pep}}$ ) indicates a decrease in the volume fraction of bulk precipitates with the addition of salt. Optical micrographs confirm the formation of (i) bulk precipitate morphologies in region I at polypeptide concentrations above  $C^*_{\text{pep}}$  and no added salt and (ii) liquid-like droplet morphologies in region V at high salinity environments above  $C^*_{\text{salt}}$ . Note that the images are from two different compositions that show distinct morphologies.

residue concentration) and 1  $\mu$ s for  $C_{\rm pep}$  = 1.0 wt % (80 mM charge residue concentration) in order to sample equilibrated configurations of the system.

The simulation results confirm that both  $\beta$ -sheet and coacervating random coil domains exist in the polypeptide complex. The most sampled conformations of the complex in the two conditions and a comparison of the radius of gyration  $(R_{\rm g})$  and the  $\beta$ -sheet content are shown in Figure 6.

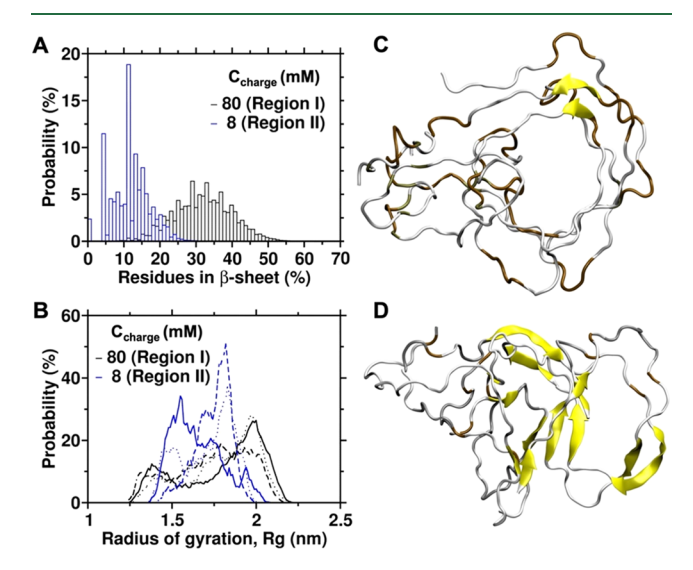


**Figure 6.** Molecular dynamic simulation of a polypeptide complex in a water box. (A) Normalized histogram of the  $\beta$ -sheet content. (B) Normalized histogram of the radius of gyration around the axes: x (solid lines), y (dotted lines), and z (dashed lines). The histograms were obtained from 0.2  $\mu$ s of simulation time. Data were collected every 10 ps. (C, D) Snapshots of the most representative structure for the 0.1 and 1.0 wt % systems, respectively, obtained by clustering structures of likely conformations according to the criteria described in the Methods Section. The structures in (C, D) were sampled over 9 and 3% of the simulation time, respectively. Amino acids participating in  $\beta$ -sheets are colored in shades of yellow and random coil sections are shown in shades of white. Yellow arrows represent sections that consist of three or more  $\beta$ -sheet-forming amino acids.

Importantly, the  $\beta$ -sheet content was found to be sensitive to the simulated polypeptide concentration (Figure 6A).  $\beta$ -Sheet content increased from  $\sim$ 6% (standard deviation: 3%) under dilute conditions (region II) to  $\sim$ 16% (standard deviation: 3%) under concentrated solution conditions (region I). The time evolution of the number of residues in the  $\beta$ -sheet conformation is shown in Figure S9. The distribution of  $R_{\rm g}$  along three orthogonal axes reflects the conformation of the complex and is plotted in Figure 6B. The time evolution of the

total radius of gyration, as well as the radius along x-, y-, and z-axes, is shown in Figure S10. The anisotropy of the molecule, characterized by differences in the value of  $R_{\rm g}$  sampled along the different molecular axes (x, y, and z, indicated by the solid, dotted, and dashed lines, respectively), is larger for  $C_{\rm pep} = 1.0$  wt % than  $C_{\rm pep} = 0.1$  wt %, indicating a more elongated and/or flatter shape for the complex at higher concentrations (Figure 6B). This result is also confirmed by the longer maximum distances observed for the complex at 1.0 wt % (Figure S11). Thus, simulations suggest that the conformation of the polypeptide complex changes from globular-like with low  $\beta$ -sheet content in region II (most sampled configuration shown in Figure 6C) to a more extended conformation with high  $\beta$ -sheet content in concentrated conditions (most sampled configuration shown in Figure 6D).

#### DISCUSSION

The results shown above indicate that the phase behavior of 1:1 charge ratio mixtures of 100-mer poly-L-lysine and poly-Lglutamic acid is sensitive to the impact of polypeptide and salt concentration on intra- and intermolecular interactions in nontrivial ways, resulting in a rich state diagram. Specifically, five regions with distinct nanoscale and macroscale morphologies are evident from combined turbidity and optical microscopy measurements. In region I, concentrated polypeptide mixtures ( $C_{pep} > C_{pep}^*$ ) form bulk precipitates (Figure 5i) with MD simulations showing that the polypeptide complex in 1 wt % solution adopts a more extended/flatter conformation accompanied by a higher  $\beta$ -sheet content (Figure 6). Conformations favor stacking with other complexes. In an experimental system at high concentration, where many complexes are present, a higher  $\beta$ -sheet content is expected due to the interaction of many complexes. These combined results suggest that intercomplex interactions enhance  $\beta$ -sheet content, resulting in nonequilibrium  $\beta$ -sheet aggregation at elevated concentrations that can result in the observed bulk precipitate morphology.

In region II, polypeptide mixtures form liquid-like coacervate droplets possessing viscoelastic rheology that resist full coalescence even after necking (Figure 2A). The droplets coalesce partially to form clustered assemblies of droplets that at higher concentrations form a sedimented network of partially coalescing droplets (Figure 3). The dynamic nature of these assemblies, even within the network phase, underscores the liquid-like mobility of the polypeptides within the dense coacervate domains. A plausible explanation for the formation of such viscoelastic assemblies is that  $\beta$ -sheet aggregates, evident in circular dichroism spectroscopy and through MD simulations, are embedded as solid-like domains within a liquid-like coacervating matrix (Figure 7). Con-

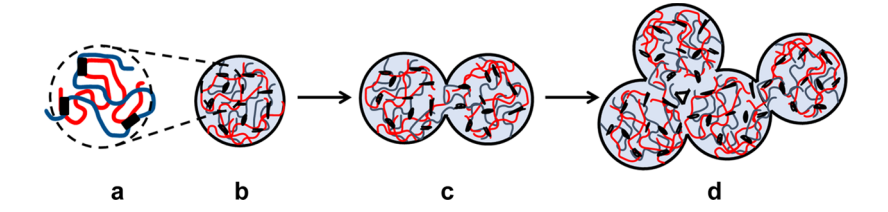


Figure 7. Schematic illustrating the hypothesized mechanism of partial coalescence. The individual polypeptide complex illustrated in (a) comprises coacervating domains (red and blue chains) and β-sheet domains (black rectangles). The complexes coacervate into liquid-like droplets with dispersed solid β-sheet domains illustrated in (b). Such droplets resist full coalescence (c), resulting in the formation of a dynamic droplet network (d).

sequently, complete coalescence driven by interfacial energy of the dense phase droplet surface is resisted by the elastic deformation energy due to the presence of a network of  $\beta$ sheet-rich domains connected by unstructured domains within the droplet. Similar phenomena involving partial coalescence are observed in fatty acid oil-in-water emulsions, wherein fat crystals contribute to a large elastic deformation energy and balance the interfacial energy driving coalescence. 45,46 In such droplets, the extent of coalescence has been shown to be dependent on the solid content and such hybrid droplets can stabilize anisotropic and aggregated assemblies of droplets. 46,47 Furthermore, Ali and Prabhu have reported a transition from liquid-like to solid-like viscoelastic rheology in hydrophobic polyelectrolyte coacervates that undergo coacervate to precipitate transition as a function of added salt. 48 In the present polypeptide system, MD simulations of the polypeptide complex indicate that a globular complex exists containing a larger fraction of coacervating domains with a random coil structure ( $\sim$ 94%) and a small fraction of  $\beta$ -sheet domains  $(\sim 6\%)$ . Thus, the simulation results corroborate experimental observations by providing molecular-scale evidence for a balance between  $\beta$ -sheet-driven molecular aggregation and bulk thermodynamic coacervation always exists within the system, but in a manner that is highly sensitive to the solution composition. Moreover, the simulations indicate that intercomplex interactions above  $C^*_{pep}$  elongate the conformation of the polypeptide complex due to the formation of stiffer  $\beta$ -sheet domains that are more rod-like.

In regions III, IV, and V, the impact of the ionic strength of the solution on the conformation of folded complexes is apparent. In region III, for dilute polypeptide concentrations  $(C_{\text{pep}} < C^*_{\text{pep}})$  and in the presence of added salt  $(C_{\text{salt}} > C_{\text{salt}}^{\#})$ , the structures formed exhibit a morphology reminiscent of colloidal aggregates of droplets that are solid-like (Figure 4i). It should be noted that polypeptide complexes can form such solid-like droplets due to salt-driven dehydration and has been reported during coacervation. 21,22 The volume fraction of colloidal aggregates in region III decreases with added salt, transitioning to a single-phase solution regime (region IV) above C\*<sub>salt</sub>. Similarly, the volume fraction of colloidal aggregates in region III increases with increasing polypeptide concentration, resulting in the formation of a volume-spanning network of droplets (Figure 4ii,iii) before transitioning into bulk precipitates in region I above  $C^*_{\text{pep}}$ . Here, a transition from loose to compact colloidal aggregates and eventually to bulk precipitates is apparent. A plausible explanation is that as the polypeptide concentration crosses the critical polypeptide concentration  $(C^*_{pep})$ , a strong overlap of polypeptide complexes and concomitant increase in hydrophobic  $\beta$ -sheet contacts results in a transition from droplets to bulk

A surprising result was observed in region V at high ionic strengths ( $C_{\rm salt} > C_{\rm salt}^*$ ) and high polypeptide concentrations ( $C_{\rm pep} > C_{\rm pep}^*$ ), wherein a re-entrant transition from a precipitated state to a state of liquid—liquid phase transition comprising dispersed coacervate droplets was observed. Low solution turbidity in this regime is consistent with the small fraction of droplets observed via optical microscopy. It is possible that differences in salt partitioning between polypeptide complexes and bulk solvent that is known to occur in coacervating systems <sup>49–51</sup> may result in phase instability under these conditions. It is important to note here that MD simulations were unable to delineate the nanostructure of the

polypeptide complexes in region V due to the absence of force fields able to reproduce such high solubility of sodium chloride salt. Specifically under similar simulation conditions with experiments, salt crystals that formed at 2 M concentrations are not compatible with a true solution of NaCl with a saturation limit of 5 M (details of force fields used here are given in the Methods Section).

#### CONCLUSIONS AND PERSPECTIVE

The subtle interplay of enthalpic interactions such as electrostatic and dispersive forces and entropic factors contributed by the restructuring of salt ions and solvent molecules are known to be critical factors during coacervation as well as misfolding of synthetic polypeptides and intrinsically disordered polypeptide domains in natural proteins.<sup>4</sup> This similarity is especially striking while considering the complex coacervation of the simplest polypeptide mixtures such as polylysine and polyglutamic acid of the same chirality (predominantly L-form in nature), which tend to form both solid-like precipitates and liquid-like coacervate droplets. 7,16 In this work, combined experiments and molecular simulations revealed a previously unreported diversity of dense morphologies in such complex coacervating polypeptide mixtures. Our findings indicate that the presence of  $\beta$ -sheet secondary structure does not guarantee precipitate formation; rather a concentration-dependent balance between propensities for nonequilibrium hydrogen bonding-driven  $\beta$ -sheet self-assembly and electrostatically dominated liquid-like coacervate formation exists within the folded polypeptide complex. From molecular-level measurements and simulations, we assess that this diversity of morphologies is primarily driven by concentration-dependent changes in the conformation and  $\beta$ sheet content of the folded polypeptide complex in the simple polypeptide mixtures.

Our results build upon previous studies identifying simple coacervate and precipitate morphologies by elucidating complex, concentration-dependent morphologies that comprise a mixture of molecular structures. Since the hydrogen bonding propensity of peptide and protein backbones has not been explicitly included in predictive theories for coacervation, 20,52 such theories fail to elucidate the rich phase behavior of the simplest of polypeptide mixtures investigated here. It is therefore not surprising that similar unanticipated morphologies have been reported for coacervate-forming intrinsically disordered peptides and proteins with more complex sequences. Therefore, it is necessary to link the balance of  $\beta$ sheet and coacervating domains, resulting conformation, and aggregation to peptide sequence and length to inform future studies of coacervating peptide mixtures with increasing complexity. In particular, advanced molecular simulations capable of accurately resolving salt solubility in high salinity conditions would resolve the particularly complex re-entrant behaviors observed in experiments,<sup>53</sup> allowing for the prediction of new hybrid morphologies emerging from welldefined materials and a controlled balance of charge interactions and backbone-driven assembly.

# ASSOCIATED CONTENT

# **Solution** Supporting Information

The Supporting Information is available free of charge at https://pubs.acs.org/doi/10.1021/acs.biomac.3c00361.

Details of NCA ROP synthesis protocols;  ${}^{1}$ H NMR, DOSY NMR, and GPC of synthesized polypeptides; CD spectra; time evolution of complex geometry and β-sheet content in MD simulations; videos of coacervating peptides (DOCX)

#### AUTHOR INFORMATION

# **Corresponding Author**

Matthew E. Helgeson – Department of Chemical Engineering, University of California Santa Barbara, Santa Barbara, California 93106, United States; oorcid.org/0000-0001-9384-4023; Email: helgeson@ucsb.edu

#### **Authors**

- Nairiti J. Sinha Department of Chemical Engineering, University of California Santa Barbara, Santa Barbara, California 93106, United States; Materials Department and Materials Research Laboratory and Department of Chemistry and Biochemistry, University of California Santa Barbara, Santa Barbara, California 93106, United States; orcid.org/0000-0003-1305-7500
- Keila Cristina Cunha Department of Chemistry and Biochemistry, University of California Santa Barbara, Santa Barbara, California 93106, United States
- Robert Murphy Department of Chemistry and Biochemistry, University of California Santa Barbara, Santa Barbara, California 93106, United States; orcid.org/0000-0003-3147-3196
- Craig J. Hawker Materials Department and Materials Research Laboratory and Department of Chemistry and Biochemistry, University of California Santa Barbara, Santa Barbara, California 93106, United States; orcid.org/ 0000-0001-9951-851X
- Joan-Emma Shea Department of Chemistry and Biochemistry, University of California Santa Barbara, Santa Barbara, California 93106, United States; orcid.org/ 0000-0002-9801-9273

Complete contact information is available at: https://pubs.acs.org/10.1021/acs.biomac.3c00361

#### **Notes**

The authors declare no competing financial interest.

#### ACKNOWLEDGMENTS

This work was supported by the MRSEC Program of the National Science Foundation under Award No. DMR-1720256 (NJS, KCC, CJH, JES and MEH, IRG-3). The research was partially supported by the BioPACIFIC Materials Innovation Platform of the National Science Foundation under Award No. DMR-1933487. The authors acknowledge the use of the Biological Nanostructures Laboratory within the California NanoSystems Institute, supported by the University of California, Santa Barbara, and the University of California, Office of the President. The authors thank Dr. Saeed Najafi, Prof. Matthew Tirrell, and Prof. Sarah Perry for insightful discussions.

# REFERENCES

(1) Wang, B.; Zhang, L.; Dai, T.; Qin, Z.; Lu, H.; Zhang, L.; Zhou, F. Liquid—Liquid Phase Separation in Human Health and Diseases. Signal Transduction Targeted Ther. 2021, 6, No. 290.

- (2) Edun, D. N.; Flanagan, M. R.; Serrano, A. L. Does Liquid–Liquid Phase Separation Drive Peptide Folding? *Chem. Sci.* **2021**, *12*, 2474–2479.
- (3) Yewdall, N. A.; André, A. A. M.; Lu, T.; Spruijt, E. Coacervates as Models of Membraneless Organelles. *Curr. Opin. Colloid Interface Sci.* **2021**, *52*, No. 101416.
- (4) Uversky, V. N. Intrinsically Disordered Proteins and Their "Mysterious" (Meta)Physics. *Front. Phys.* **2019**, *7*, 1–23.
- (5) Mason, A. F.; van Hest, J. C. M. Multifaceted Cell Mimicry in Coacervate-Based Synthetic Cells. *Emerging Top. Life Sci.* **2019**, *3*, 567–571.
- (6) Abbas, M.; Lipiński, W. P.; Wang, J.; Spruijt, E. Peptide-Based Coacervates as Biomimetic Protocells. *Chem. Soc. Rev.* **2021**, *50*, 3690–3705.
- (7) Cakmak, F. P.; Choi, S.; Meyer, M. O.; Bevilacqua, P. C.; Keating, C. D. Prebiotically-Relevant Low Polyion Multivalency Can Improve Functionality of Membraneless Compartments. *Nat. Commun.* **2020**, *11*, No. 5949.
- (8) Perry, S. L.; Sing, C. E. 100th Anniversary of Macromolecular Science Viewpoint: Opportunities in the Physics of Sequence-Defined Polymers. *ACS Macro Lett.* **2020**, *9*, 216–225.
- (9) Sing, C. E.; Perry, S. L. Recent Progress in the Science of Complex Coacervation. *Soft Matter* **2020**, *16*, 2885–2914.
- (10) Kaminker, I.; Wei, W.; Schrader, A. M.; Talmon, Y.; Valentine, M. T.; Israelachvili, J. N.; Waite, J. H.; Han, S. Simple Peptide Coacervates Adapted for Rapid Pressure-Sensitive Wet Adhesion. *Soft Matter* **2017**, *13*, 9122–9131.
- (11) Priftis, D.; Tirrell, M. Phase Behaviour and Complex Coacervation of Aqueous Polypeptide Solutions. *Soft Matter* **2012**, 8, 9396–9405.
- (12) Priftis, D.; Farina, R.; Tirrell, M. Interfacial Energy of Polypeptide Complex Coacervates Measured via Capillary Adhesion. *Langmuir* **2012**, 28, 8721–8729.
- (13) Shea, J.-E.; Best, R. B.; Mittal, J. Physics-Based Computational and Theoretical Approaches to Intrinsically Disordered Proteins. *Curr. Opin. Struct. Biol.* **2021**, *67*, 219–225.
- (14) Tabandeh, S.; Leon, L. Engineering Peptide-Based Polyelectrolyte Complexes with Increased Hydrophobicity. *Molecules* **2019**, 24, No. 868.
- (15) Wang, Y.; Lomakin, A.; Kanai, S.; Alex, R.; Benedek, G. B. Liquid–Liquid Phase Separation in Oligomeric Peptide Solutions. *Langmuir* **2017**, 33, 7715–7721.
- (16) Perry, S. L.; Leon, L.; Hoffmann, K. Q.; Kade, M. J.; Priftis, D.; Black, K. A.; Wong, D.; Klein, R. A.; Pierce, C. F.; Margossian, K. O.; Whitmer, J. K.; Qin, J.; De Pablo, J. J.; Tirrell, M. Chirality-Selected Phase Behaviour in Ionic Polypeptide Complexes. *Nat. Commun.* **2015**, *6*, No. 6052.
- (17) Wu, H.; Ting, J. M.; Werba, O.; Meng, S.; Tirrell, M. V. Non-Equilibrium Phenomena and Kinetic Pathways in Self-Assembled Polyelectrolyte Complexes. *J. Chem. Phys.* **2018**, *149*, No. 163330.
- (18) Donau, C.; Späth, F.; Sosson, M.; Kriebisch, B. A. K.; Schnitter, F.; Tena-Solsona, M.; Kang, H. S.; Salibi, E.; Sattler, M.; Mutschler, H.; Boekhoven, J. Active Coacervate Droplets as a Model for Membraneless Organelles and Protocells. *Nat. Commun.* **2020**, *11*, No. 5167.
- (19) Park, S.; Barnes, R.; Lin, Y.; Jeon, B. j.; Najafi, S.; Delaney, K. T.; Fredrickson, G. H.; Shea, J. E.; Hwang, D. S.; Han, S. Dehydration Entropy Drives Liquid-Liquid Phase Separation by Molecular Crowding. *Commun. Chem.* **2020**, *3*, No. 83.
- (20) Danielsen, S. P. O.; McCarty, J.; Shea, J.-E.; Delaney, K. T.; Fredrickson, G. H. Molecular Design of Self-Coacervation Phenomena in Block Polyampholytes. *Proc. Natl. Acad. Sci. U.S.A.* **2019**, *116*, 8224–8232.
- (21) Singh, A. N.; Yethiraj, A. Driving Force for the Complexation of Charged Polypeptides. *J. Phys. Chem. B* **2020**, *124*, 1285–1292.
- (22) Tsanai, M.; Frederix, P. W. J. M.; Schroer, C. F. E.; Souza, P. C. T.; Marrink, S. J. Coacervate Formation Studied by Explicit Solvent Coarse-Grain Molecular Dynamics with the Martini Model. *Chem. Sci.* **2021**, *12*, 8521–8530.

- (23) Dobson, C. M. Principles of Protein Folding, Misfolding and Aggregation. Semin. Cell Dev. Biol. 2004, 15, 3-16.
- (24) Kono, H.; Saven, J. G. Statistical Theory for Protein Combinatorial Libraries. Packing Interactions, Backbone Flexibility, and the Sequence Variability of a Main-Chain Structure11Edited by J. Thornton. J. Mol. Biol. 2001, 306, 607–628.
- (25) Saven, J. G. Combinatorial Protein Design. Curr. Opin. Struct. Biol. 2002, 12, 453-458.
- (26) Marciel, A. B.; Srivastava, S.; Tirrell, M. V. Structure and Rheology of Polyelectrolyte Complex Coacervates. *Soft Matter* **2018**, 14, 2454–2464.
- (27) Pacalin, N. M.; Leon, L.; Tirrell, M. Directing the Phase Behavior of Polyelectrolyte Complexes Using Chiral Patterned Peptides. *Eur. Phys. J.: Spec. Top.* **2016**, 225, 1805–1815.
- (28) Tian, Z.-Y.; Zhang, Z.; Wang, S.; Lu, H. A Moisture-Tolerant Route to Unprotected  $\alpha/\beta$ -Amino Acid N-Carboxyanhydrides and Facile Synthesis of Hyperbranched Polypeptides. *Nat. Commun.* **2021**, 12, No. 5810.
- (29) Wu, Y.; Zhang, D.; Ma, P.; Zhou, R.; Hua, L.; Liu, R. Lithium Hexamethyldisilazide Initiated Superfast Ring Opening Polymerization of Alpha-Amino Acid N-Carboxyanhydrides. *Nat. Commun.* **2018**, *9*, No. 5297.
- (30) Schindelin, J.; Arganda-Carreras, I.; Frise, E.; Kaynig, V.; Longair, M.; Pietzsch, T.; Preibisch, S.; Rueden, C.; Saalfeld, S.; Schmid, B.; Tinevez, J.-Y.; White, D. J.; Hartenstein, V.; Eliceiri, K.; Tomancak, P.; Cardona, A. Fiji: An Open-Source Platform for Biological-Image Analysis. *Nat. Methods* **2012**, *9*, 676–682.
- (31) Berendsen, H. J. C.; Postma, J. P. M.; van Gunsteren, W. F.; Hermans, J. Interaction Models for Water in Relation to Protein Hydration. In *Intermolecular Forces*, Proceedings of the Fourteenth 538 Jerusalem Symposium on Quantum Chemistry and Biochemistry Held in Jerusalem, Israel, April 539 13–16; Pullman, B., Ed.; Springer: Dordrecht, Netherlands, 1981; pp 331–342.
- (32) Loche, P.; Steinbrunner, P.; Friedowitz, S.; Netz, R. R.; Bonthuis, D. J. Transferable Ion Force Fields in Water from a Simultaneous Optimization of Ion Solvation and Ion—Ion Interaction. *J. Phys. Chem. B* **2021**, *125*, 8581–8587.
- (33) Oostenbrink, C.; Villa, A.; Mark, A. E.; Van Gunsteren, W. F. A Biomolecular Force Field Based on the Free Enthalpy of Hydration and Solvation: The GROMOS Force-Field Parameter Sets 53A5 and 53A6. *J. Comput. Chem.* **2004**, *25*, 1656–1676.
- (34) Miyamoto, S.; Kollman, P. A. Settle: An Analytical Version of the SHAKE and RATTLE Algorithm for Rigid Water Models. *J. Comput. Chem.* **1992**, *13*, 952–962.
- (35) Darden, T.; York, D.; Pedersen, L. Particle Mesh Ewald: An N-log(N) Method for Ewald Sums in Large Systems. *J. Chem. Phys.* 1993, 98, 10089–10092.
- (36) Essmann, U.; Perera, L.; Berkowitz, M. L.; Darden, T.; Lee, H.; Pedersen, L. G. A Smooth Particle Mesh Ewald Method. *J. Chem. Phys.* **1995**, *103*, 8577–8593.
- (37) Verlet, L. Computer "Experiments" on Classical Fluids. I. Thermodynamical Properties of Lennard-Jones Molecules. *Phys. Rev.* **1967**, *159*, 98–103.
- (38) Daura, X.; Gademann, K.; Jaun, B.; Seebach, D.; van Gunsteren, W. F.; Mark, A. E. Peptide Folding: When Simulation Meets Experiment. *Angew. Chem., Int. Ed.* **1999**, *38*, 236–240.
- (39) Kabsch, W.; Sander, C. Dictionary of Protein Secondary Structure: Pattern Recognition of Hydrogen-Bonded and Geometrical Features. *Biopolymers* **1983**, *22*, 2577–2637.
- (40) Touw, W. G.; Baakman, C.; Black, J.; te Beek, T. A. H.; Krieger, E.; Joosten, R. P.; Vriend, G. A Series of PDB-Related Databanks for Everyday Needs. *Nucleic Acids Res.* **2015**, *43*, D364–D368.
- (41) Mazo, A. R.; Allison-Logan, S.; Karimi, F.; Chan, N. J.-A.; Qiu, W.; Duan, W.; O'Brien-Simpson, N. M.; Qiao, G. G. Ring Opening Polymerization of  $\alpha$ -Amino Acids: Advances in Synthesis, Architecture and Applications of Polypeptides and Their Hybrids. *Chem. Soc. Rev.* **2020**, *49*, 4737–4834.

- (42) Cox, J. P. L.; Evans, P. A.; Packman, L. C.; Williams, D. H.; Woolfson, D. N. Dissecting the Structure of a Partially Folded Protein. *J. Mol. Biol.* **1993**, 234, 483–492.
- (43) Domard, A.; Rinaudo, M. Polyelectrolyte Complexes. Interaction of Poly(L-Lysine)-Poly(L-Glutamic Acid) in Dilute Aqueous Solution. *Macromolecules* **1980**, *13*, 898–904.
- (44) Muthukumar, M. 50th Anniversary Perspective: A Perspective on Polyelectrolyte Solutions. *Macromolecules* **2017**, *50*, 9528–9560.
- (45) Pawar, A. B.; Caggioni, M.; Hartel, W.; Spicer, P. T.; Hartel, R. W.; Spicer, P. T. Arrested Coalescence of Viscoelastic Droplets with Internal Microstructure. *Faraday Discuss.* **2012**, *158*, 341–350.
- (46) Thiel, A. E.; Hartel, R. W.; Spicer, P. T.; Hendrickson, K. J. Coalescence Behavior of Pure and Natural Fat Droplets Characterized via Micromanipulation. *J. Am. Oil Chem. Soc.* **2016**, 93, 1467–1477.
- (47) Caggioni, M.; Bayles, A. V.; Lenis, J.; Furst, E. M.; Spicer, P. T. Interfacial Stability and Shape Change of Anisotropic Endoskeleton Droplets. *Soft Matter* **2014**, *10*, 7647–7652.
- (48) Ali, S.; Prabhu, V. Relaxation Behavior by Time-Salt and Time-Temperature Superpositions of Polyelectrolyte Complexes from Coacervate to Precipitate. *Gels* **2018**, *4*, No. 11.
- (49) Luo, Y.; Gu, M.; Edwards, C. E. R.; Valentine, M. T.; Helgeson, M. E. High-Throughput Microscopy to Determine Morphology, Microrheology, and Phase Boundaries Applied to Phase Separating Coacervates. *Soft Matter* **2022**, *18*, 3063–3075.
- (50) Sing, C. E. Development of the Modern Theory of Polymeric Complex Coacervation. *Adv. Colloid Interface Sci.* **2017**, 239, 2–16.
- (51) Li, L.; Srivastava, S.; Andreev, M.; Marciel, A. B.; de Pablo, J. J.; Tirrell, M. V. Phase Behavior and Salt Partitioning in Polyelectrolyte Complex Coacervates. *Macromolecules* **2018**, *51*, 2988–2995.
- (52) Rumyantsev, A. M.; Kramarenko, E. Y.; Borisov, O. V. Microphase Separation in Complex Coacervate Due to Incompatibility between Polyanion and Polycation. *Macromolecules* **2018**, *51*, 6587–6601.
- (53) Hong, Y.; Najafi, S.; Casey, T.; Shea, J.-E.; Han, S.-I.; Hwang, D. S. Hydrophobicity of Arginine Leads to Reentrant Liquid-Liquid Phase Separation Behaviors of Arginine-Rich Proteins. *Nat. Commun.* **2022**, *13*, No. 7326.

ı